Afterbody Drag Reduction Using Active Flow Control

R. Jackson[1], Z. Wang[2] and I. Gursul[3]
Department of Mechanical Engineering, University of Bath, Bath, BA2 7AY, UK

Experiments were performed in a water tunnel to assess the efficacy of blowing via pairs of circular and high aspect ratio slot jets to modify the counter-rotating vortices in the near-wake of a slanted base cylinder. Drag force and crossflow Particle Image Velocimetry measurements were collected. Drag reductions achieved by circular jets on the upswept face were highly dependent on blowing direction and location. These reductions reached close to 7% when blowing outboard at further upstream and inboard locations, caused by jet vortices restricting the shear layer development, which lead to smaller vortex cores further from the surface. Upstream blowing into the vortex cores produced highly diffuse vortices at the trailing-edge, as a result of a reduction in peak instantaneous vorticity and increased meandering. Surface-normal slot blowing from the upswept face had little effect on the afterbody flow field, while spanwise blowing from the upsweep edge deflected the vortices away from the surface, but at the expense of increasing the drag coefficient. A jet flap nearly parallel to the freestream achieved drag reductions close to 9%, equating to energy savings of almost 3%. Jet vortices shortened the shear layer, resulting in weaker afterbody vortices with smaller cores and lower circulation. Instantaneous analysis revealed reduced separation on the upswept surface, and less turbulent kinetic energy in the vortices.

Nomenclature

A_j	=	cross-sectional area of jet	x	=	streamwise distance
c	=	chord length of upswept face	x_j	=	streamwise jet location
C_D	=	drag coefficient	x'	=	local co-ordinate along upswept face
C_μ	=	jet momentum coefficient, $\dot{m}_j U_j / 0.5\rho U_\infty^2 S$	x'_j	=	jet location on upswept face
D	=	diameter of fuselage	y	=	normal distance
L	=	length of afterbody	z	=	spanwise distance
$\dot{m}_j$	=	mass flow of jet, $\rho A_j U_j$	z_j	=	spanwise jet location
P	=	drag power, $C_D 0.5\rho U_\infty^3 S$	α_j	=	jet incidence angle
P_{in}	=	jet power, $0.5\dot{m}_j U_j^2$	β_j	=	jet yaw angle
P_{net}	=	net power savings	Γ	=	vortex circulation
Re_D	=	Reynolds number, $\rho U_\infty D/\mu$	μ	=	dynamic viscosity
S	=	cross-sectional area of fuselage	ρ	=	density
U_j	=	jet velocity	σ	=	root-mean-square meandering amplitude
U_∞	=	freestream velocity	φ	=	upsweep angle
V	=	crossflow velocity magnitude	ω	=	vorticity

I. Introduction

To allow for their rear-loading capability, many military transport aircraft are designed with a steep upsweep angle. The Lockheed Martin C-130 'Hercules' has an upsweep angle of $\varphi = 28°$, compared with the shallower upsweeps of civilian passenger aircraft in the range of $12° < \varphi < 16°$. Previous studies have used simplified fuselage models to demonstrate that an aircraft with a larger upsweep angle has an inherently larger drag coefficient, indicating that this problem is more pertinent to cargo aircraft[1,2]. It has been suggested that the afterbody drag may contribute towards a significant portion of the total aircraft drag[3].

Flow field analysis has previously shown that an upsweep angle in the range $0° < \varphi < 45°$ promotes three-dimensional flow separation, leading to a reduction in the pressure on the upswept surface and the formation of a counter-rotating vortex pair[4-6]. The low pressure on the upswept face causes a reduction in lift, in addition to an

[1] Postgraduate Research Student, Dept. of Mechanical Engineering, Student Member AIAA.
[2] Lecturer, Dept. of Mechanical Engineering.
[3] Professor of Aerospace Engineering, Dept. of Mechanical Engineering, Associate Fellow AIAA.

increase in drag[2,7]. Furthermore, the vortices are capable of disrupting the initial path of payloads and paratroopers during airdrop missions.

Several passive flow control solutions have demonstrated reductions in drag coefficient. One of the earliest examples dates back to the 1960s, where vertical strakes were mounted close to the edge of the upsweep of the Short Belfast. The aim was to reduce inflow to the vortex pair, thereby delaying their formation. Results indicated drag reductions of up to 7%[8]. However, it was identified that up to half of the potential drag reduction was lost through the parasitic drag of the strakes themselves. These strakes can also limit airdrop capabilities. Other passive methods have included arrays of co-rotating and counter-rotating vortex generators. These were either mounted on the fuselage underside upstream of the upsweep, or along the edge of the fuselage breakline extending aft towards the tail[9-11]. The vortices produced by the vortex generators were designed to delay separation and weaken the afterbody vortices. The drag coefficient was reduced by up to 6% in some cases, with a strong dependency on geometry and arrangement.

There is limited evidence of the efficacy of active flow control techniques when applied to the afterbody vortex problem. Steady blowing outboard via a pair of circular jets was recently shown to be successful at weakening the afterbody vortices, causing them to appear more diffuse near the trailing-edge as a result of increased meandering[6]. Other examples of vortex modification using active flow control include turbulence ingestion to diffuse wing tip vortices in the near-wake[12,13]. The degree of control was shown to be highly dependent on blowing location, direction and C_μ. Spanwise and surface-normal wing tip blowing can also result in the diffusion of the wing tip vortex, but through its destructive interaction with the generated jet vortex[14,15]. In addition, spanwise blowing can deflect the tip vortex to a position further from the wing surface[16]. Like upswept aircraft afterbodies, the rear slant on Ahmed bodies induces flow separation and the formation of a counter-rotating vortex pair. Significant drag reductions worth over 10% have been demonstrated on Ahmed bodies using steady and pulsed blowing from slot jets and microjet arrays on the slant surface[17-19]. These examples were shown to be effective at reducing boundary layer separation, increasing the surface pressure on the slant and weakening the vortex pair.

The aims of this study were to measure the change in drag coefficient and net energy savings of an upswept axisymmetric cylinder, through direct force measurements, when activating steady blowing via a pair of circular jets and slot jets. The effect of the position and direction of the circular jets on the upswept surface was varied. Spanwise, surface-normal and streamwise blowing was performed for different slot jet configurations. Experiments were performed in a water tunnel and the flow field was captured using Particle Image Velocimetry (PIV).

II. Experimental Methods

A. Experimental Setup

The model which generated the flow field of interest is a slanted-base axisymmetric cylinder, used as an approximation of an upswept fuselage. The model has an ellipsoidal nose and a flat upswept face at an angle of φ = 28°, which is within the range of many military transport aircraft. The diameter of the model is D = 89 mm and the afterbody fineness ratio is L/D = 1.88. An overview of the model parameters is outlined in Fig. 1. The energy for the blowing jets was provided by a pressurized air supply. The water delivery system fed into a plenum chamber, which was located behind the upswept face, and served as a settling chamber before ejecting water out through the jets. The jet momentum coefficient, C_μ, was controlled using a variable area flowmeter.

PIV and drag force measurements were collected in a free-surface, closed-loop water tunnel. The tunnel has a test section of width 381 mm and height 508 mm where flow can reach a maximum freestream velocity of 0.5 m/s. The turbulence intensity has previously been measured using Laser Doppler Velocimetry to be less than 0.5% across the flow velocity range. The Reynolds number of the flow was based on fuselage diameter and fixed at Re_D = 20,000, resulting in a freestream velocity of around U_∞ = 0.25 m/s. The estimated uncertainty in setting the freestream velocity is ±2%. An overview of the experimental setup is presented in Fig. 2.

B. Force Measurements

The high weight-to-drag ratio of the model was such that a traditional bending beam force balance was not able to accurately measure the low drag forces (~ 0.1 N) while also providing a structural support. The required low second moment of area for a bending beam meant that there would be significant beam deflection (and risk of breakage) even from small moments caused by the weight of the model. A Futek ‘S Beam’ load cell with a capacity of 0.5 N was used to measure the drag force. This was fixed in-situ at one end while the other end was free to deflect under load. The free end was attached to a carriage which was supported by two rails, parallel to the freestream, each of which passed through a pair of air bearings. The model was attached to the carriage. Any moments were absorbed by the bearings, ensuring that the model weight was isolated during drag force measurements. A zero

reading was collected with U_∞ = 0 m/s before and after each experiment. The drift between zero readings was typically measured to be less than 1% of the baseline measurement, suggesting insignificant friction in the bearings. The data for the baseline and flow control cases were collected for 90 seconds at a sampling rate of 500 Hz. An end plate was placed on the top of the tunnel such that it was just submerged beneath the free-surface in order to prevent wave oscillations being transmitted to the load cell.

The drag change is defined as $\Delta C_D = C_{D1} - C_{D0}$ (where subscripts 0 and 1 are the baseline and flow control conditions, respectively). Hence, ΔC_D is negative for drag reductions. The power saved due to drag reduction can be defined as:

$$\Delta P = \Delta C_D \frac{1}{2} \rho U_\infty^3 S \,. \tag{1}$$

Assuming that the flow in the plenum chamber is at rest and that there is negligible change in potential and pressure energy, then the power supplied to the jet is:

$$P_{in} = \frac{1}{2} \dot{m}_j U_j^2 \,. \tag{2}$$

The energy balance is then considered by the net power savings, $P_{net}=\Delta P+P_{in}$. If this is normalized by $P_{D0} = C_{D0}0.5\rho U_\infty^3 S$, then:

$$\frac{P_{net}}{P_{D0}} = \frac{\Delta P + P_{in}}{P_{D0}} = \frac{\Delta C_D}{C_{D0}} + \frac{C_\mu}{C_{D0}} \frac{U_j}{2U_\infty}, \tag{3}$$

where $C_\mu = \dot{m}_j U_j / 0.5\rho U_\infty^2 S$. Therefore, the net energy balance is dependent on the drag reduction, jet momentum coefficient and velocity ratio. The uncertainty in the drag reduction, $\Delta C_D/C_{D0}$, was estimated to be ±0.5%, using the Constant Odds Combination method introduced by Moffat[20]. Similarly, the uncertainty in net energy savings, P_{net}/P_{D0}, was estimated to be ±1.0%.

C. PIV Measurements

Crossflow PIV measurements were collected at five equidistant stations along the afterbody length (x/L = {0.2, 0.4, 0.6, 0.8, 1.0}), as shown in Fig. 1c. A 4MP 12-bit digital CCD camera captured the images at a rate of 15 Hz and this was positioned downstream of the tunnel, facing the afterbody. Spherical glass particles with diameters of 8 µm to 12 µm were used to seed the flow, and these were illuminated using a 120 mJ dual-head Nd:YAG laser which generated a sheet of light approximately 1 mm thick. The operation of the laser and camera was controlled using a TSI Model 610034 synchronizer. Time-averaged results were processed from 500 pairs of images collected at each streamwise station. The processor used the Hart correlation algorithm with an interrogation window of 32 x 32 pixels and 50% overlap, which resulted in a vector resolution of less than 1% of the model diameter.

D. Jet Parameters

The range of blowing jet designs that were tested are described below. The total jet momentum coefficient was set constant at C_μ = 0.02 for all cases.

1. Circular jets

A pair of 1 mm diameter circular jets were moulded in discs to allow for simple manual control of the jet yaw angle. The jets were positioned on the upswept surface and were symmetric about the z = 0 plane as demonstrated in Fig. 3a for one example jet position. The chordwise (x'_j/c) and spanwise (z_j/D) jet locations were varied, in addition to the jet incidence (α_j) and yaw angles (β_j). The tested chordwise jet locations were x'_j/c = {0.12, 0.2, 0.3, 0.4}. The spanwise spacing between the different stations was 5 mm, equivalent to $\Delta z_j/D$ = 0.056. The numbered jet locations are shown in Fig. 3b, with the majority outboard of the vortex core (shown by the dashed trajectory), to increase the likelihood of disrupting vortex formation. The jet numbers are ordered outboard to inboard, bottom to top. The definition of the jet incidence and yaw angles is depicted in Fig. 3c. The jet velocity was approximately U_j = 1.6 m/s, giving a velocity ratio of around U_j/U_∞ = 6.4.

2. Surface-normal slot jets

A pair of slot jets of length 30 mm and width 0.5 mm were positioned on the upswept face, close to the edge of the upsweep, and symmetric about the z = 0 plane. The jets exited normal to the surface, as shown in Fig. 4a. The

jets extended from (x'_j/c = 0.1, z_j/D = ±0.236) to (x'_j/c = 0.25, z_j/D = ±0.357). The location of the slots is outlined in Fig. 4b. The velocity ratio was U_j/U_∞ = 1.5.

3. Jet flap

A jet flap was positioned close to the upstream apex of the slant at x'_j/c = 0.07, with the aim of minimizing flow separation on the upswept face, as previously shown on other bodies with slanted bases[17]. The jet incidence angle was varied, which is defined in Fig. 5a. The slot spanned 30 mm and had a width of 0.5 mm. Its location relative to the baseline vortex trajectory is shown in Fig. 5b. The velocity ratio of the jet flap was U_j/U_∞ = 2.1.

4. Spanwise slot jets

A pair of slot jets of width 0.5 mm were positioned on either side of the afterbody, parallel to the upsweep edge, and offset by 2.5 mm. They extended from x_j/L = 0.1 to x_j/L = 0.25, each with a length of 28.5 mm. The location of one of the slots and the direction of the jets are shown in Fig. 6a and Fig. 6b, respectively. The aim of the jet was to disrupt the shear layer. The velocity ratio of the slot jets was U_j/U_∞ = 1.6.

III. Results and Discussion

A. Circular jets

1. Force data

The effect of the spanwise and streamwise location of the pair of circular jets was first tested for three different jet directions: α_j = 30°, β_j = 0° (outboard blowing), α_j = 30°, β_j = 90° (streamwise blowing) and α_j = 90° (surface-normal blowing). Outboard blowing has previously demonstrated diffusion of the afterbody vortex pair[6], while there is evidence that streamwise and surface-normal blowing can attenuate wing tip vortices[12,13,14,15]. Figure 7 demonstrates the influence of blowing location and the three jet directions on the reduction in drag coefficient as a percentage of the baseline. Outboard blowing (Fig. 7a) is most effective at Location 3, where a drag reduction of $\Delta C_D/C_{D0}$ = -4.8% is achieved. The benefit reduces with further aft and further outboard jet locations. Blowing in the streamwise direction (Fig. 7b) is more beneficial at further outboard locations, but is less dependent on streamwise position. Significant reductions of between $\Delta C_D/C_{D0}$ = -5% and $\Delta C_D/C_{D0}$ = -7% are demonstrated at several locations. Jets blowing perpendicular to the surface (Fig. 7c) are shown to be the least effective at reducing the drag, with a maximum reduction of $\Delta C_D/C_{D0}$ = -2.7% noted and with little variation across the test region.

A study into the effect of β_j was undertaken to identify if there are additional jet yaw angles at which further reductions can be achieved. For these experiments, the jet pitch angle was fixed at α_j = 30°. Figure 8 demonstrates the effect of β_j at Locations 2, 3 6 and 10. The drag reductions at these stations are compared with the theoretical component of jet thrust in the x-direction to reveal improvements due to favorable jet/vortex interactions (Fig. 8a). Blowing outboard from Location 3 adds a significant benefit on to the theoretical jet thrust component. The most significant additional benefit occurs for jets with β_j = 270° through to β_j = 90°. The greatest reduction occurs at β_j = 30°, where the total drag reduction is $\Delta C_D/C_{D0}$ = -6.7%. At the outboard and downstream stations of Location 2 and 6, the benefits of blowing outboard are no longer achieved. The drag reduction matches closely with the theoretical model, aside from some cases of upstream blowing. However, the overall improvement due to upstream blowing is negligible for all stations. The corresponding net energy is calculated from Equation 3 and is shown in Fig. 8b. This is compared against the net energy if the drag reduction was purely from the theoretical thrust. The net energy increase ranges from P_{net}/P_{D0} = 9% to P_{net}/P_{D0} = 17% across the test cases. One reason for the significant energy increase is the high jet velocity.

2. PIV data

The time-averaged vorticity field of an outboard blowing case at Location 3, α_j = 30°, β_j = 0°, is compared against the baseline in Fig. 9. The jet interaction with the afterbody flow field generates a pair of counter-rotating vortices, which initially prevent the shear layer from developing too far inboard, as shown at x/L = 0.2 (Fig. 9a). The developing vortices at x/L = 0.4 are restricted to positions further outboard and with smaller vortex cores (Fig. 9b). This is also the case at x/L = 0.6 and x/L = 0.8, where the vortex centers have moved further away from the upswept surface (Fig. 9c and Fig. 9d). The resultant vortices at the trailing-edge appear more diffuse (Fig. 9e).

Figure 10 presents the time-averaged vorticity field for an upstream blowing case into the vortex cores, with the direction of the jets opposing the vortex trajectories (Location 10, α_j = 30°, β_j = 247°). At x/L = 0.2 (Fig. 10a), the shear layer is greatly weakened, before the vortices form with smaller cores (Fig. 10b and Fig. 10c). The vortices are much more diffuse at further downstream locations of x/L = 0.8 and x/L = 1.0, showing symptoms of vortex breakdown (Fig. 10d and Fig. 10e). However, there is a small drag increase of $\Delta C_D/C_{D0}$ = 0.8% (Fig. 8a), which is

partly expected to be because of the drag penalty of the jet. Drag increases aside, a potential advantage of upstream blowing is to dissipate the vorticity, which may alleviate any deviations in the trajectory of payloads during airdrop missions caused by the swirling flow in the afterbody vortices.

The root-mean-square (RMS) crossflow velocity of the flow field for the baseline case is compared against the outboard and upstream blowing cases in Fig. 11. Only the three most upstream stations are shown. For the baseline case, the turbulence arises from instabilities in the shear layer at x/L = 0.4 and x/L = 0.6. Very little turbulence is observed in the afterbody vortex cores. For outboard blowing, the jet vortices exhibit a region of turbulence at x/L = 0.2. Further downstream, the RMS velocity within the afterbody vortex shear layer is reduced. The unsteadiness caused by the jet vortices is still evidenced at x/L = 0.4 and x/L = 0.6, inboard of the afterbody vortex cores. Upstream blowing generates a much more intense region of turbulence at x/L = 0.4, which leads to the dissipation of vorticity further downstream.

The circulation of the time-averaged vortex pair is presented in Fig. 12 for the two jet directions, from x/L = 0.4 through to the trailing-edge. The jet/vortex interactions cause a reduction in circulation for both cases at x/L = 0.4 and x/L = 0.6, before the circulation recovers to baseline levels at the trailing-edge. The circulation reduces by 10% at x/L = 0.6 with upstream blowing (Fig. 12b). The reductions can be attributed to the smaller vortex cores at these upstream stations shown in Fig. 9 and Fig. 10.

To assess the effect of flow control on the instantaneous flow field, the maximum vorticity of both the time-averaged and ensemble-averaged instantaneous left vortex is plotted against streamwise distance in Fig. 13. The center of the instantaneous vortex is found from the location of minimum velocity. For outboard blowing (Fig. 13a), the instantaneous vortex is strengthened at x/L = 0.4 and x/L = 0.6. However, the circulation here is lower due in part to the smaller vortex core seen in Fig. 9b and Fig. 9c. The time-averaged vortex has a larger peak vorticity at these upstream stations. The time-averaged and instantaneous vortex are only weakened slightly at the trailing-edge. With upstream blowing, the instantaneous vortex at x/L = 0.4 is strengthened (Fig. 13b), but the instantaneous vortices downstream at x/L = 0.8 and x/L = 1.0 are greatly weakened. The peak time-averaged vorticity is also reduced.

Figure 14 presents the RMS meandering amplitude in both the vertical and spanwise directions for the vortex pair, following outboard and upstream blowing. As before, the minimum velocity criteria is used to define the location of the instantaneous vortex. Meandering along the y axis of the baseline vortex increases slightly with streamwise distance, while it reduces along the z axis. This is reflected in the time-averaged vortex changing from elliptical to circular in structure. With outboard blowing (Fig. 14a and Fig. 14b), the meandering amplitude along both axes is reduced at x/L = 0.4 and x/L = 0.6, and it increases slightly at the trailing-edge. With upstream blowing (Fig. 14c and Fig. 14d), the meandering amplitude is significantly increased at x/L = 0.6 and stations further downstream. Coupled with a reduction in peak instantaneous vorticity, this explains the highly diffuse time-averaged vortex in Fig. 10d and Fig. 10e.

B. Surface-normal slot jets

A drag reduction of $\Delta C_D/C_{D0}$ = -0.6% was measured for the surface-normal slot blowing case defined in Fig. 4, but with a corresponding net energy increase of P_{net}/P_{D0} = 3.6%. The reduction in drag coefficient is noticeably less than the $\Delta C_D/C_{D0}$ = -2.7% achieved with the pair of circular jets blowing normal to the surface (Fig. 7c). The expected drag reduction from the theoretical jet thrust is $\Delta C_D/C_{D0}$ = -2.4%, suggesting that there is an adverse effect caused by the slot jets. Four other jet slot lengths were tested in addition to the example case in Fig. 4. The slots of differing length and starting location were positioned along the line defined by the coordinates (x'_j/c = 0.1, z_j/D = ±0.236) and (x'_j/c = 0.3, z_j/D = ±0.405). For these additional slots, the drag reduction varied between $\Delta C_D/C_{D0}$ = -0.6% and $\Delta C_D/C_{D0}$ = -1.8%, and the net energy increase between P_{net}/P_{D0} = 2.8% and P_{net}/P_{D0} = 3.1%.

The time-averaged vorticity field for the case described in Fig. 4 is presented in Fig. 15. The intersection of the jet with the shear layer is seen at x/L = 0.2 (Fig. 15a) and a secondary shear layer develops from the interaction between the jet and afterbody flow. The vortex has a slightly smaller core at x/L = 0.4 (Fig. 15b), and appears more diffuse at x/L = 0.6 and x/L = 0.8 (Fig. 15c and Fig. 15d), before re-strengthening at the trailing-edge (Fig. 15e). Figure 16 shows that there is a small reduction in circulation at x/L = 0.4 and x/L = 0.6, before it recovers at the trailing-edge. One reason for the smaller than expected drag reductions may be the stronger (albeit shorter) shear layer at x/L = 0.2 (Fig. 15a) inducing a lower pressure on the upswept surface.

C. Jet flap

The effect of the jet flap incidence angle on the drag reduction and net energy savings is shown in Fig. 17, and compared against the contribution from the theoretical jet thrust component. Generally, with increasing upsweep angle, the drag reductions (and subsequent energy savings) reduce. The greatest improvement in the drag coefficient occurs for α_j = 30°, when the jet is almost parallel to the freestream. At this angle, the drag reduction totals $\Delta C_D/C_{D0}$

= -8.6%, with a corresponding net energy reduction of P_{net}/P_{D0} = -2.8%. At angles greater than α_j = 45°, the measured drag and energy reductions are less than the thrust contributions. For larger angles, there is a risk that the jet is deflecting the streamlines away as the flow passes the upstream apex of the upsweep, thereby increasing the width of the wake.

The time-averaged vorticity field for the α_j = 30° jet flap case is shown in Fig. 18. At x/L = 0.2 (Fig. 18a), jet vortices generated at the tips of the jet flap restrict the formation of the developing shear layer such that it is shorter, but more intense, than the baseline. The size of the vortex cores at x/L = 0.4 (Fig. 18b) and x/L = 0.6 (Fig. 18c) are reduced, with the vortices displaced slightly away from the surface, similar to that seen in the flow field for outboard blowing from circular jets (Fig. 9). There is little difference in the peak vorticity between the baseline and flow control cases at x/L = 0.8 (Fig. 18d) and at the trailing-edge (Fig. 18e), but the size of the vortex cores appears slightly reduced.

The comparison between the turbulence intensity of the baseline and jet flap cases in Fig. 19 shows that there is reduced shear layer instability at x/L = 0.4 (Fig. 19b) and x/L = 0.6 (Fig. 19c) when the jet flap is activated. There is also less separation close to the vertical plane of symmetry on the upswept surface at x/L = 0.4 and x/L = 0.6. This reduced separation compares to that seen in surface-normal blowing from spanwise microjets on Ahmed bodies[17].

Figure 20 shows that circulation of the time-averaged vortex is noticeably reduced across all streamwise stations including the trailing-edge, with reductions of over 16% at x/L = 0.4. This lower vortex circulation, coupled with a displacement away from the upswept surface, is likely to result in an increased surface pressure, leading to the significant drag reductions that were measured.

D. Spanwise slot jets

For the spanwise slot blowing case defined in Fig. 6, the drag coefficient increased by $\Delta C_D/C_{D0}$ = 5.0%, with a corresponding net energy increase of P_{net}/P_{D0} = 9.2%. The drag coefficient of eight additional slots were tested, of lengths ranging from 19 mm to 47.5 mm, and which were positioned between x/L = 0.05 and x/L = 0.3, along an extension of the line defining the slot in Fig. 6. For these cases, the increase in drag coefficient ranged between $\Delta C_D/C_{D0}$ = 4.0% and $\Delta C_D/C_{D0}$ = 7.4%, with the net energy increasing between P_{net}/P_{D0} = 8.7% and P_{net}/P_{D0} = 11.3%.

The time-averaged flow field for the case described in Fig. 6 is presented in Fig. 21. The spanwise blowing from the jets causes the outer edge of the shear layer to form further outboard, beyond the edge of the upsweep (Fig. 21a). The resultant shear layer appears to have two regions of concentrated vorticity. The subsequent afterbody vortices at x/L = 0.4 (Fig. 21b) appear more diffuse and disorganized, particularly the right vortex. The vortex cores at x/L = 0.4 and x/L = 0.6 (Fig. 21c) are deflected away from the upswept face, as also observed with wing tip vortices following spanwise blowing from the tips[14,16]. The vortices at the final two stations appear more diffuse. The increase in drag coefficient is expected to be a result of the deflection of streamlines away from the surface of the upsweep in the spanwise direction, thereby increasing the area of the wake.

The effect of the spanwise jets on the RMS velocity is shown in Fig. 22. The turbulence intensity increases significantly at x/L = 0.2 (Fig. 22a), highlighting the instability in the shear layer. At x/L = 0.4 and x/L = 0.6, the shear layer instability reduces, but interestingly there is more turbulence inboard of the vortex cores, which extends further downwards than for the baseline case (Fig. 22b and Fig. 22c). This may be caused by the merging of both parts of the broken shear layer. There is little difference in flow separation along the symmetry plane on the upswept surface between both cases.

The smaller, more diffuse vortices at x/L = 0.4 (Fig. 21b) result in the reduction in circulation observed in Fig. 23. However, the total circulation increases downstream by a greater rate than the baseline, such that the circulation at the trailing-edge is higher.

IV. Conclusions

An experimental study has been performed into the efficacy of blowing via pairs of circular and high aspect ratio slot jets to control the counter-rotating vortices in the near-wake of a slanted base cylinder. This was quantified in terms of drag reductions and energy savings. For circular jets, the drag reduction was highly dependent upon the blowing direction and position on the upswept face. The most significant benefits were achieved when blowing outboard at further upstream and inboard locations, totaling drag reductions close to $\Delta C_D/C_{D0}$ = -7%. Outboard blowing was shown to generate a pair of jet vortices, which restricted the shear layer development, leading to smaller afterbody vortex cores further from the surface. Although blowing upstream into the vortex core increased the drag coefficient, the afterbody vortices experienced significant diffusion, caused by a reduction in peak instantaneous vorticity and increased meandering. For all circular jet cases that were tested, more energy was invested compared to that which was saved, due in part to the high jet velocity.

Surface-normal slot blowing resulted in small drag reductions of $\Delta C_D/C_{D0} \geq$ -2% for a range of slot lengths. The net energy was less sensitive to slot length, and remained around P_{net}/P_{D0} = 3%. The flow field structure and vortex strength were very similar to the baseline for one example case. A jet flap angled α_j = 30° to the surface achieved the largest drag reductions out of all incidence angles tested, totaling close to $\Delta C_D/C_{D0}$ = -9%, and equating to energy savings worth around P_{net}/P_{D0} = -3%. For this case, jet vortices caused a shorter shear layer, resulting in weaker afterbody vortices with smaller cores and reduced circulation. Instantaneous analysis revealed less separation on the upswept surface, and lower turbulent kinetic energy in the vortices. Spanwise slot blowing resulted in drag increases of $\Delta C_D/C_{D0} \geq$ 4% for a range of slot lengths, corresponding to net energy increases of $P_{net}/P_{D0} \geq$ 7%. The flow field for an example case showed that a broken shear layer formed with increased turbulent kinetic energy and increased wake area. The stronger shear layer is likely to generate extra suction, even though the vortices were deflected from the surface at further downstream locations.

Planned work involves further investigation of the design parameters of the jet flap, including streamwise position and span. A study into the jet momentum coefficient will also be performed. Once the geometric parameters of the jet flap have been optimized, the effect of pulsing the jet will be explored (in order to reduce the input energy), and volumetric measurements will be collected for the most promising cases.

Acknowledgements

This research is sponsored by the AFOSR, under the grant number FA9550-14-1-0126.

References

[1]Bearman, P. W., "Bluff Body Flows Applicable to Vehicle Aerodynamics," *Journal of Fluids Engineering*, Vol. 102, No. 3, 1980, pp. 265-274.

[2]Bulathsinghala, D., Wang, Z., and Gursul, I., "Effect of Upsweep Angle on Afterbody Vortices," AIAA-2016-4344, *AIAA 46th Fluid Dynamics Conference*, AIAA, Reston, VA, 2016.

[3]Thomas, A. S., Saric, W. S., Braslow, A. L., Bushnell, D. M., Lock, R. C. and Hackett, J. E., "Aircraft Drag Prediction and Reduction," *AGARD Report No. 723*, 1985, pp. 1-6.

[4]Epstein, R. J., Carbonaro, M. C., and Caudron, F., "Experimental Investigation of the Flowfield About an Upswept Afterbody," *Journal of Aircraft*, Vol. 31, No. 6, 1994, pp. 1281-1290.

[5]Bury, Y., Jardin, T. and Klockner, A., "Experimental Investigation of the Vortical Activity in the Close Wake of a Simplified Military Transport Aircraft," *Experiments in Fluids*, Vol. 54, No. 5, 2013, pp. 1-15.

[6]Jackson, R., Wang, Z., and Gursul, I., "Control of Afterbody Vortices by Blowing," AIAA-2015-2777, *AIAA 45th Fluid Dynamics Conference*, AIAA, Reston, VA, 2015.

[7]Britcher, C. P., and Alcorn, C. W., "Interference-Free Measurements of the Subsonic Aerodynamics of Slanted-Base Ogive Cylinders," *AIAA Journal*, Vol. 29, No. 4, 1991, pp. 520-525.

[8]McCluney, B. and Marshall, J., "Drag Development of the Belfast," *Aircraft Engineering and Aerospace Technology*, Vol. 39, No. 10, 1967, pp. 33-37.

[9]Calarese, W., Crisler, W. P., and Gustafson, G. L., "Afterbody Drag Reduction by Vortex Generators," AIAA-1985-0354, *AIAA 23rd Aerospace Sciences Meeting*, AIAA, New York, NY, 1985.

[10]Wortman, A., "Reduction of Fuselage Form Drag by Vortex Flows," *Journal of Aircraft*, Vol. 36, No. 3, 1999, pp. 501-506.

[11]Smith, B. R., Yagle, P. J. and Hooker, J. R., "Reduction of Aft Fuselage Drag on the C-130 Using Microvanes," AIAA-2013-0105, *AIAA 51st Aerospace Sciences Meeting*, AIAA, Reston, VA, 2013.

[12]Phillips, W. R. C., and Graham, J. A. H., "Reynolds-Stress Measurements in a Turbulent Trailing Vortex," *Journal of Fluid Mechanics*, Vol. 147, Oct., 1984, pp. 353-371.

[13]Margaris, P., Marles, D., and Gursul, I., "Experiments on Jet/Vortex Interaction," *Experiments in Fluids*, Vol. 44, No. 2, 2008, pp. 261-278.

[14]Margaris, P., and Gursul, I., "Vortex Topology of Wing Tip Blowing," *Aerospace Science and Technology*, Vol. 14, No. 3, 2010, pp. 143-160.

[15]Hu, T., Wang, Z., and Gursul, I., "Passive Control of Roll Oscillations of Low-Aspect-Ratio Wings Using Bleed," *Experiments in Fluids*, Vol. 55, No. 6, 2014, pp. 1-16.

[16]Heyes, A., and Smith, D., "Spatial Perturbation of a Wing-tip Vortex Using Pulsed Span-wise Jets," *Experiments in Fluids*, Vol. 37, No. 1, 2004, pp. 120-127.

[17]Aubrun, S., McNally, J., Alvi, F., and Kourta, A., "Separation Flow Control on a Generic Ground Vehicle Using Steady Microjet Arrays," *Experiments in Fluids*, Vol. 51, No. 5, 2011, pp. 1177-1187.

[18]Joseph, P., Amandolese, X., and Aider, J., "Drag Reduction on the 25 Degree Slant Angle Ahmed Reference Body Using Pulsed Jets," *Experiments in Fluids*, Vol. 52, No. 5, 2012, pp. 1169-1185.

[19]Gillieron, P., and Kourta, A., "Aerodynamic Drag Control by Pulsed Jets on Simplified Car Geometry," *Experiments in Fluids*, Vol. 52, No. 2, 2013, pp. 1-16.

[20]Moffat, R.J., "Describing the Uncertainties in Experimental Results," *Experimental Thermal and Fluid Science*, Vol. 1, No. 1, 1988, pp. 3-17.

Figures

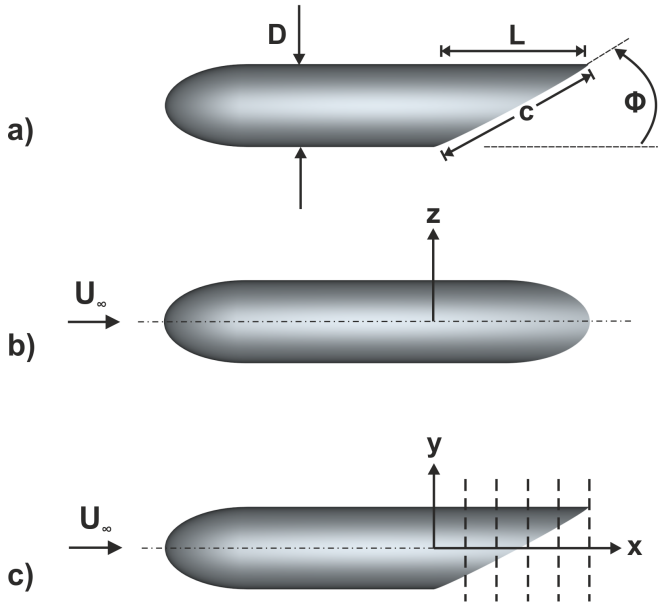

Figure 1. Outline of the simplified fuselage model showing (a), definitions of the basic dimensions on the side view; (b) and (c), the axes on the top-down and side views, respectively. The crossflow measurement planes are indicated in (c) by vertical dashed lines.

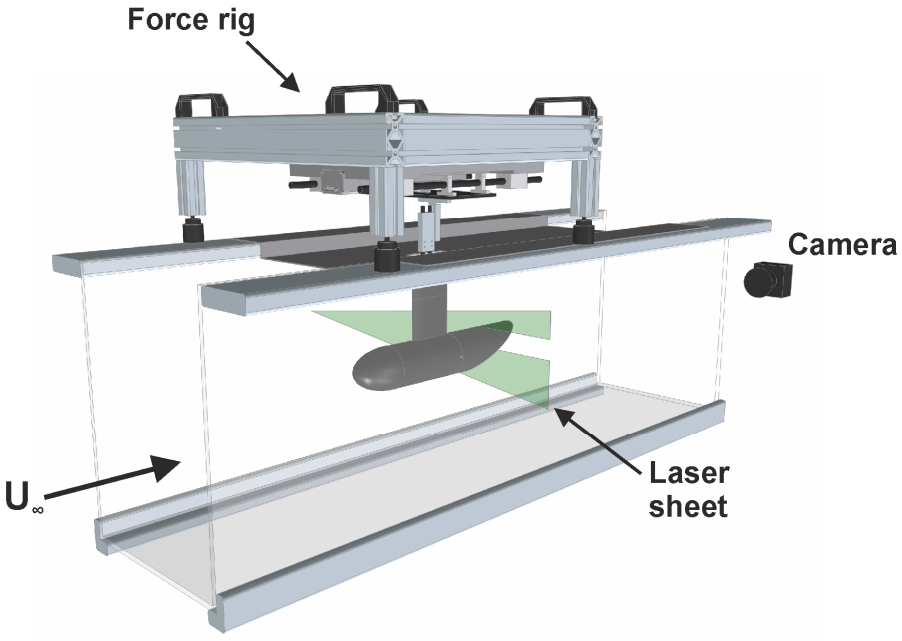

Figure 2. A schematic of the experimental setup in the water tunnel.

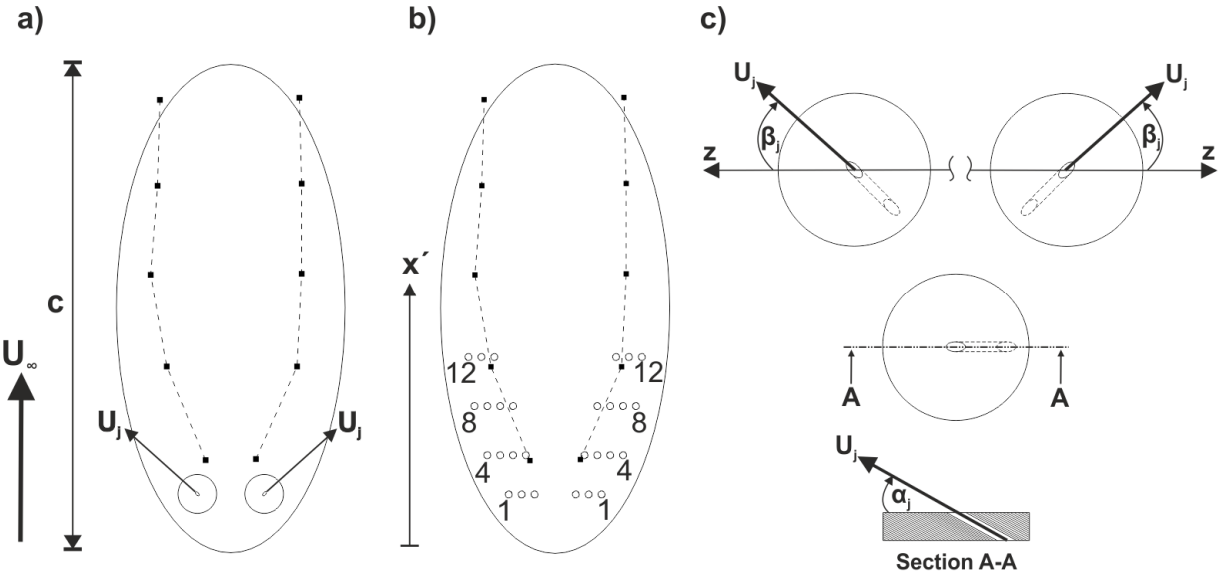

Figure 3. Key parameters for the circular jet configurations, showing a) the upswept face and the vortex trajectory for the baseline case, with one of the jet locations for reference; b) the positions of the different jet locations tested, numbered outboard to inboard, bottom to top; c) the definition of the yaw and incidence angles for the jets.

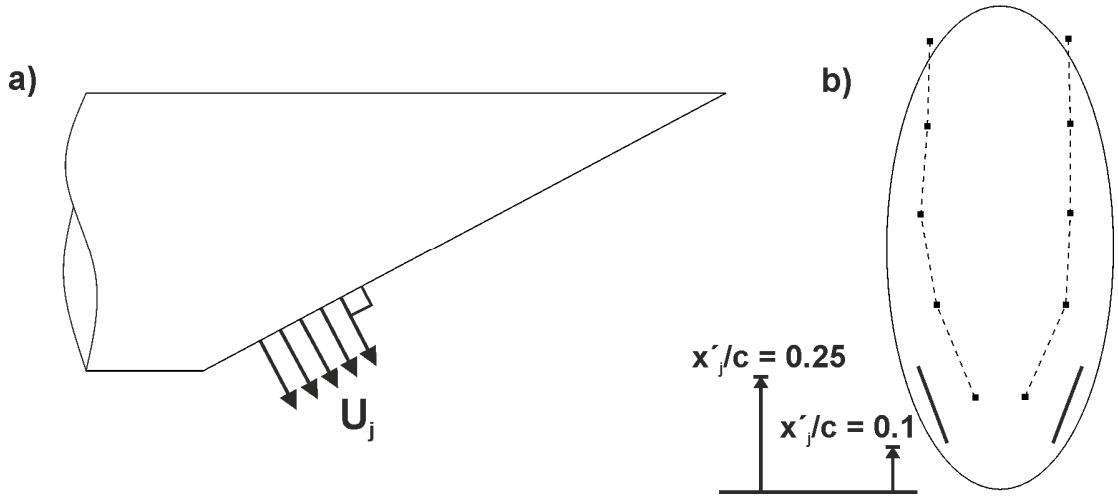

Figure 4. Definition of the surface-normal slot jets showing (a) the direction of the jets on the side view of the afterbody, and (b) the location of the slot jets on the upswept face and the vortex trajectory for the baseline case.

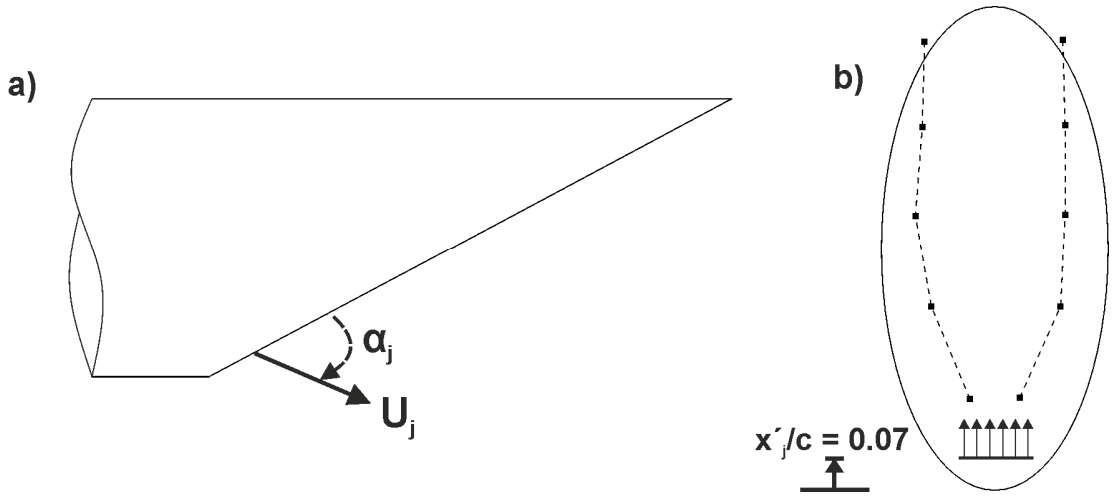

Figure 5. Definition of the jet flap showing (a) the incidence angle of the jet on the side view of the afterbody, and (b) the location of the jet flap on the upswept face and the vortex trajectory for the baseline case.

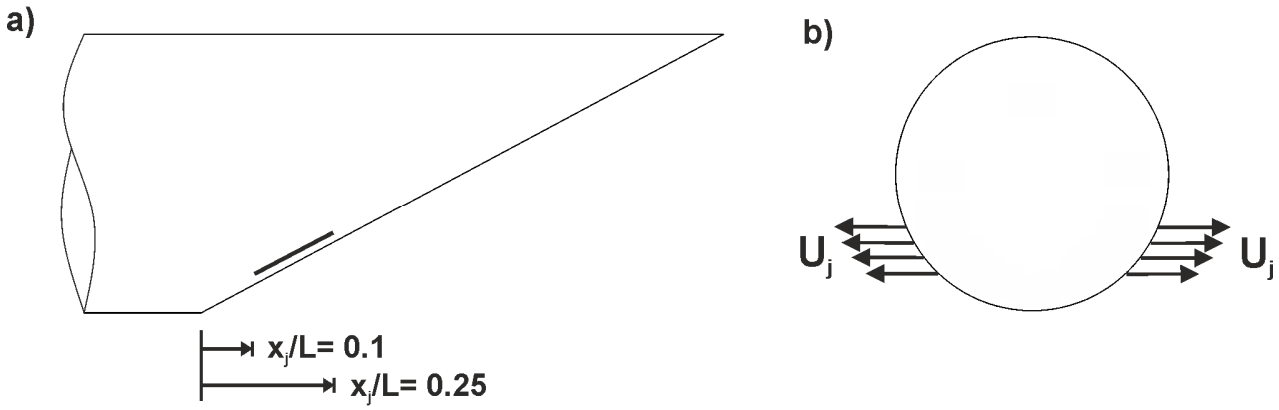

Figure 6. Definition of the spanwise slot jets showing (a) the location of one of the slot jets on the side view of the afterbody, and (b) the direction of the jets viewed from downstream.

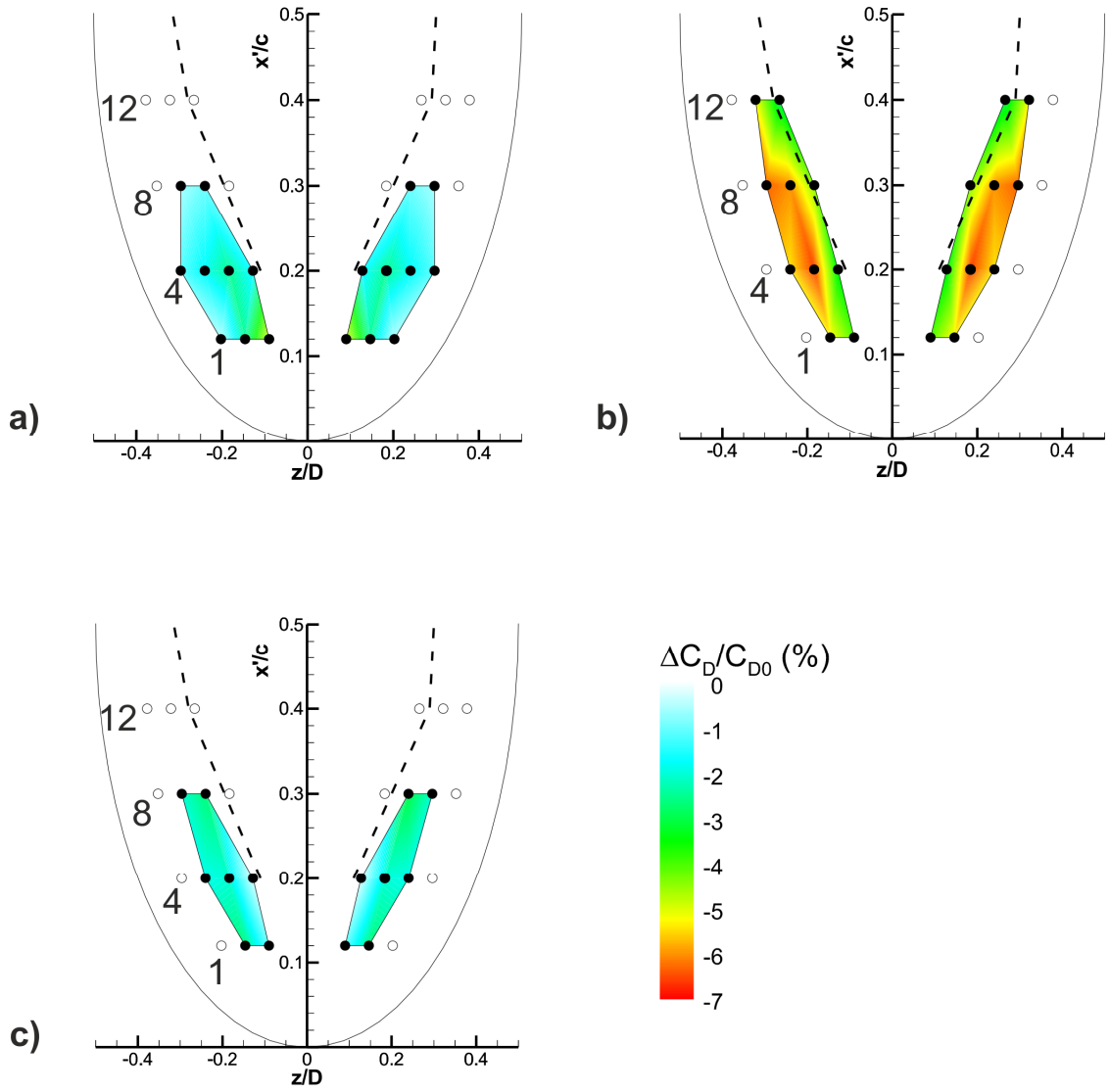

Figure 7. Drag reduction from circular jets as a function of jet location for three different jet directions: a) α_j = 30°, β_j = 0°; b) α_j = 30°, β_j = 90° and c) α_j = 90°. Filled holes indicate collected data. Jet location is numbered outboard to inboard, bottom to top.

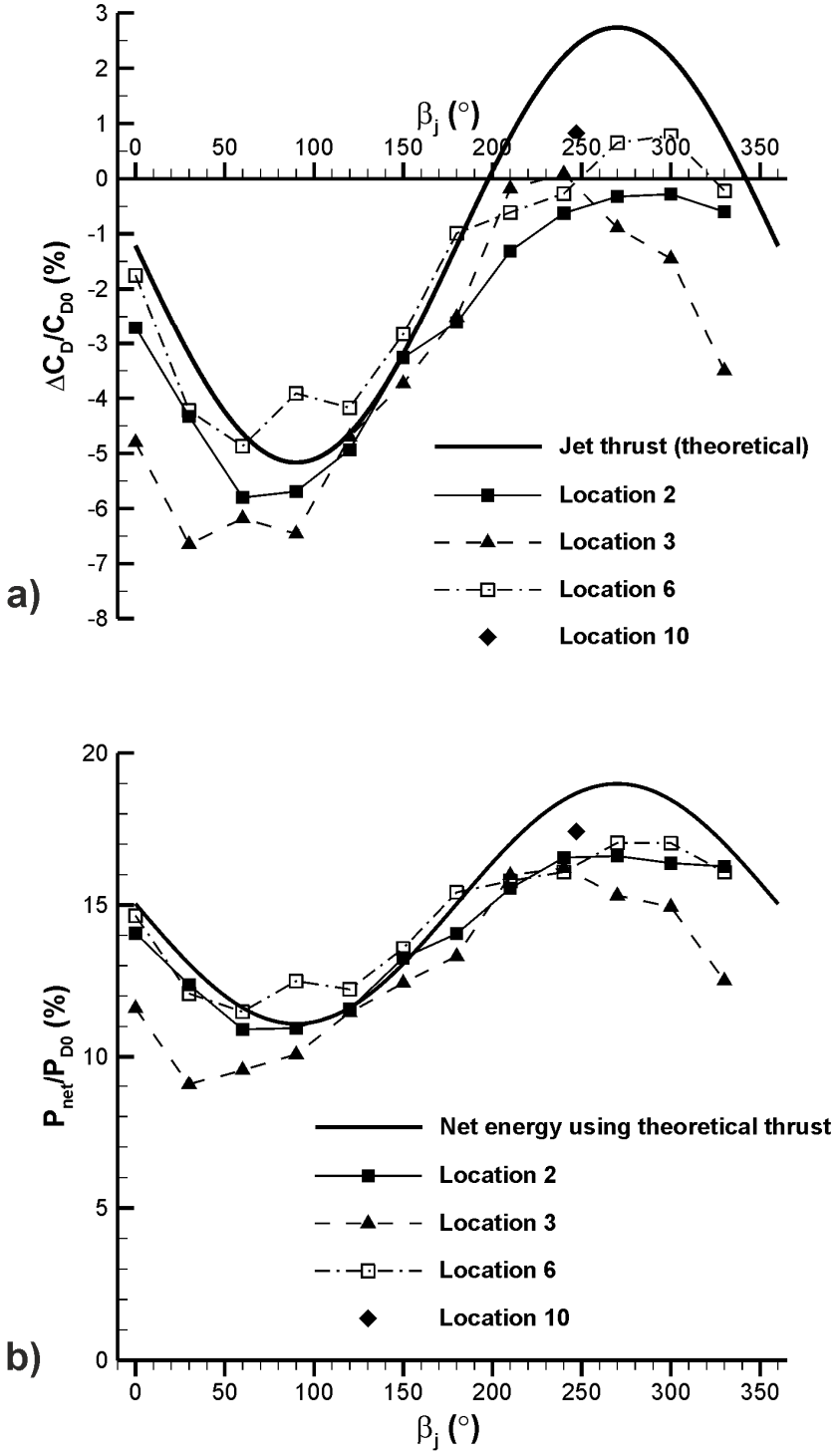

Figure 8. Effect of circular jet yaw angle, β_j, on (a) the change in drag coefficient and (b) net energy for four different jet locations. The theoretical jet thrust is determined by resolving the x-component of C_μ and dividing through by the baseline drag coefficient, C_{D0}.

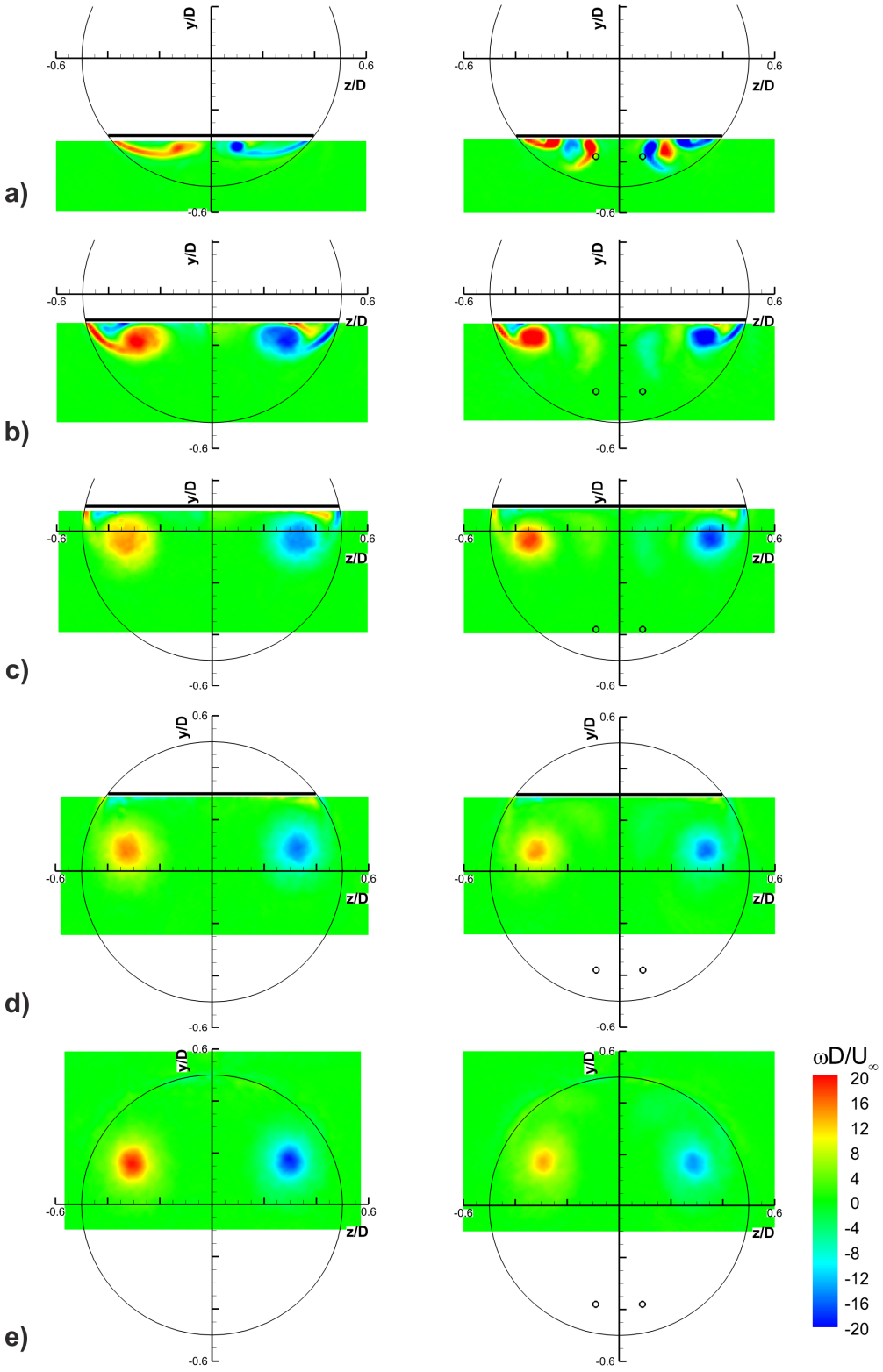

Figure 9. Time-averaged crossflow vorticity of the baseline case, left, and outboard blowing case (Location 3, $\alpha_j = 30°$, $\beta_j = 0°$), right. Jet positions are indicated by small, black circles. Measurement planes are located at a) x/L = 0.2, b) x/L = 0.4, c) x/L = 0.6, d) x/L = 0.8 and e) x/L = 1.0.

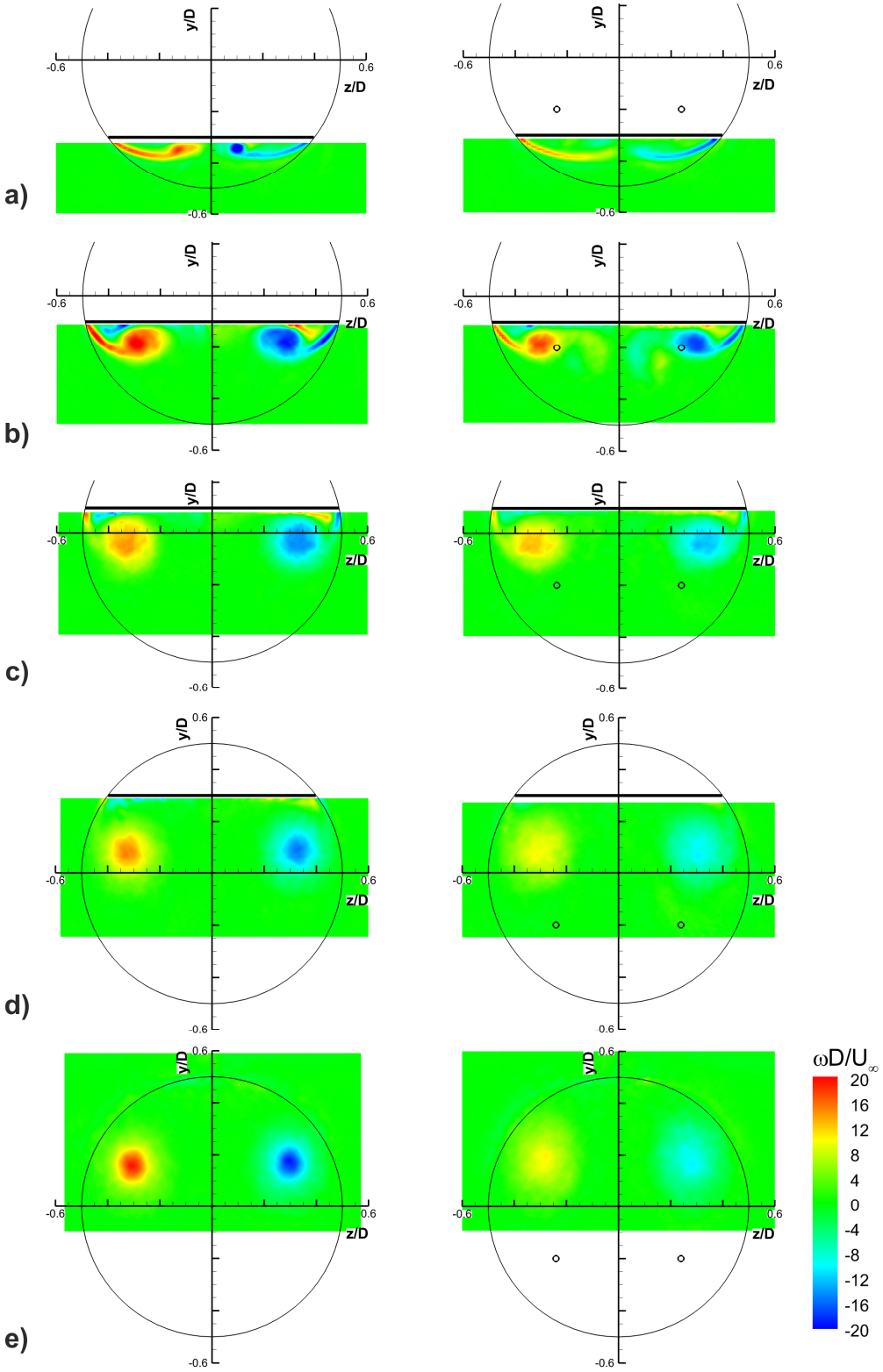

Figure 10. Time-averaged crossflow vorticity of the baseline case, left, and upstream blowing case (Location 10, $\alpha_j = 30°$, $\beta_j = 247°$), right. Jet positions are indicated by small, black circles. Measurement planes are located at a) x/L = 0.2, b) x/L = 0.4, c) x/L = 0.6, d) x/L = 0.8 and e) x/L = 1.0.

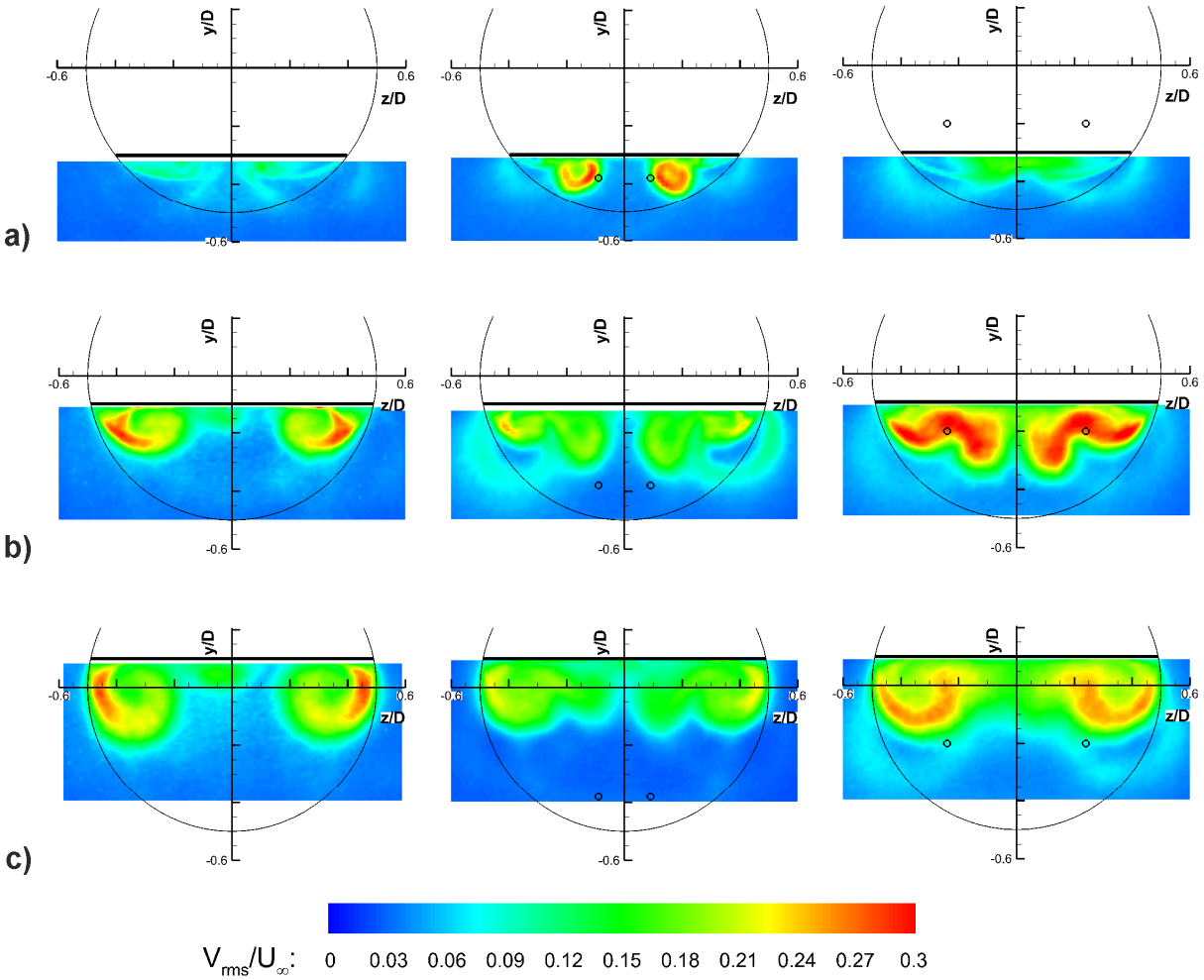

Figure 11. Crossflow turbulence intensity of the baseline case, left, outboard blowing case, middle, and upstream blowing case, right. Jet positions are indicated by small, black circles. Measurement planes are located at a) x/L = 0.2, b) x/L = 0.4 and c) x/L = 0.6.

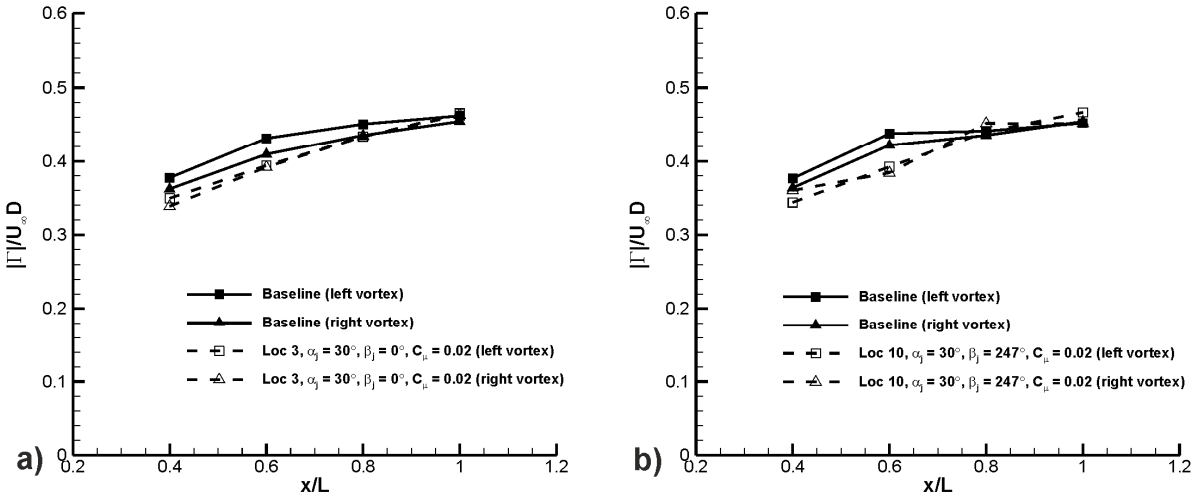

Figure 12. Development of crossflow vortex circulation with streamwise distance for a) the outboard blowing case and b) the upstream blowing case.

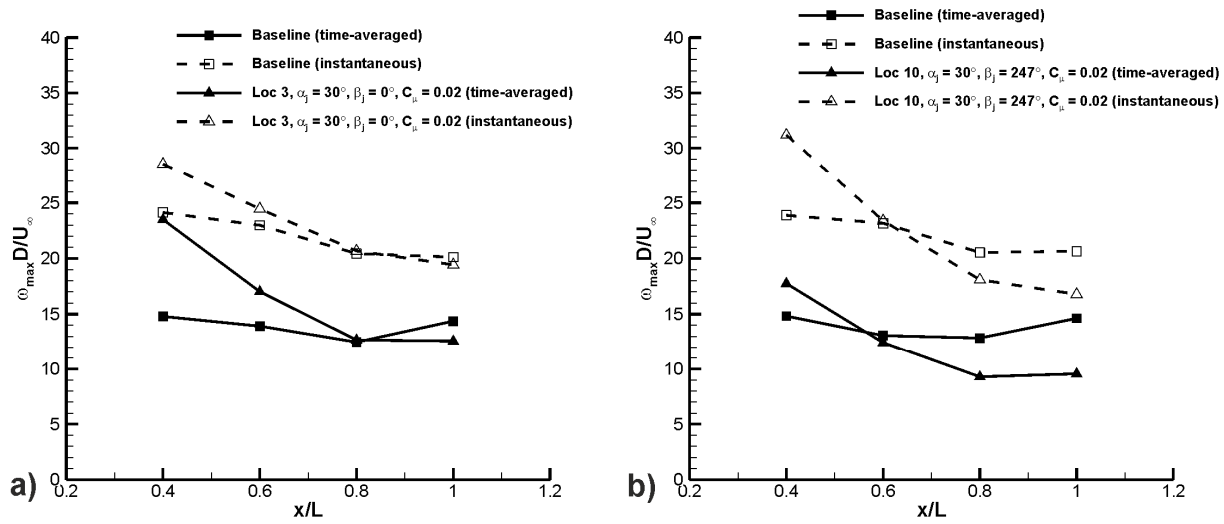

Figure 13. Variation of maximum crossflow vorticity of the left vortex with streamwise distance for a) the outboard blowing case and b) the upstream blowing case.

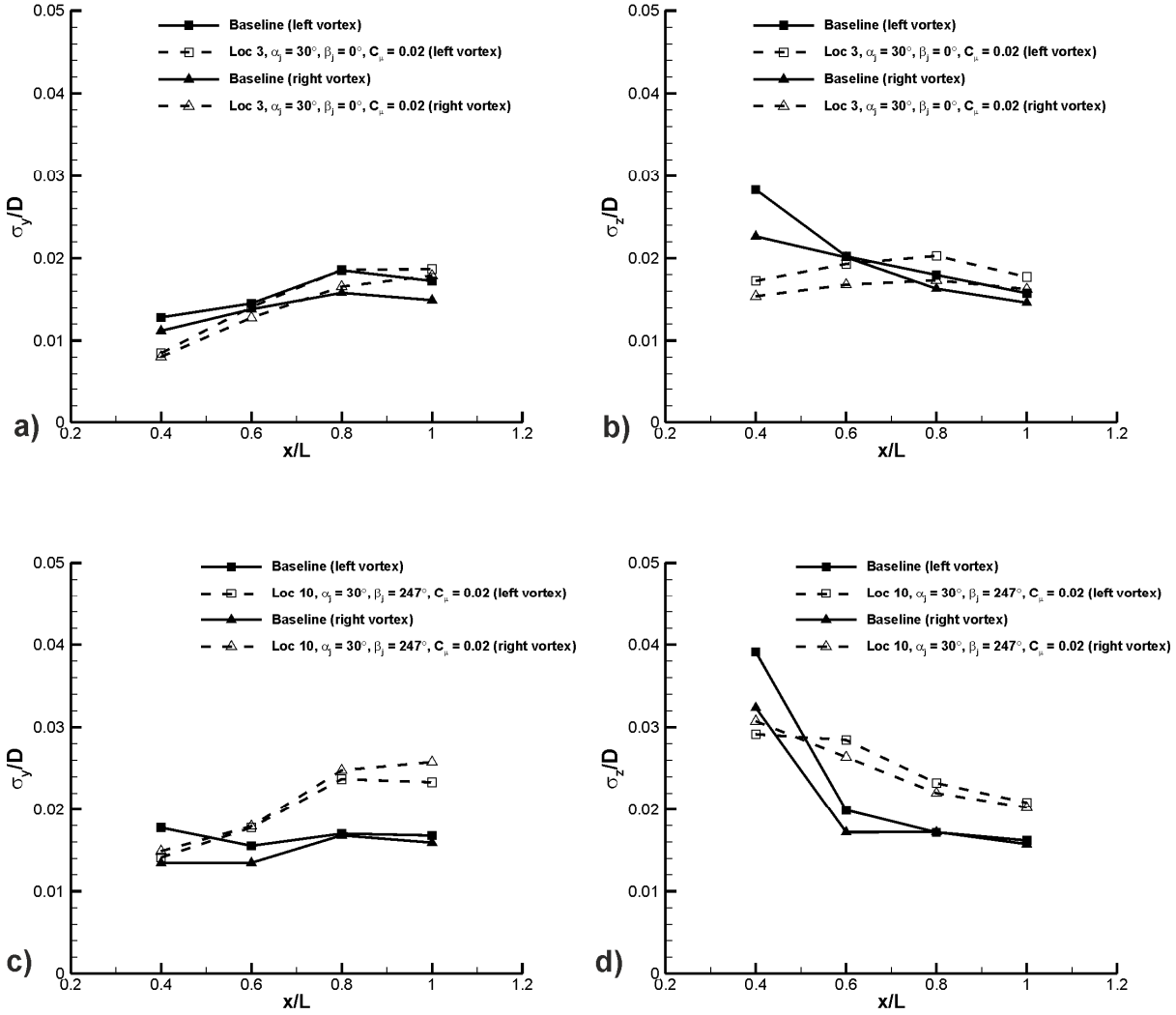

Figure 14. Variation in RMS vortex meandering amplitude with streamwise distance for the outboard and upstream blowing cases. Meandering in the vertical and spanwise directions for the outboard blowing case is presented in a) and b), respectively. Meandering for the upstream blowing case is shown in c) and d).

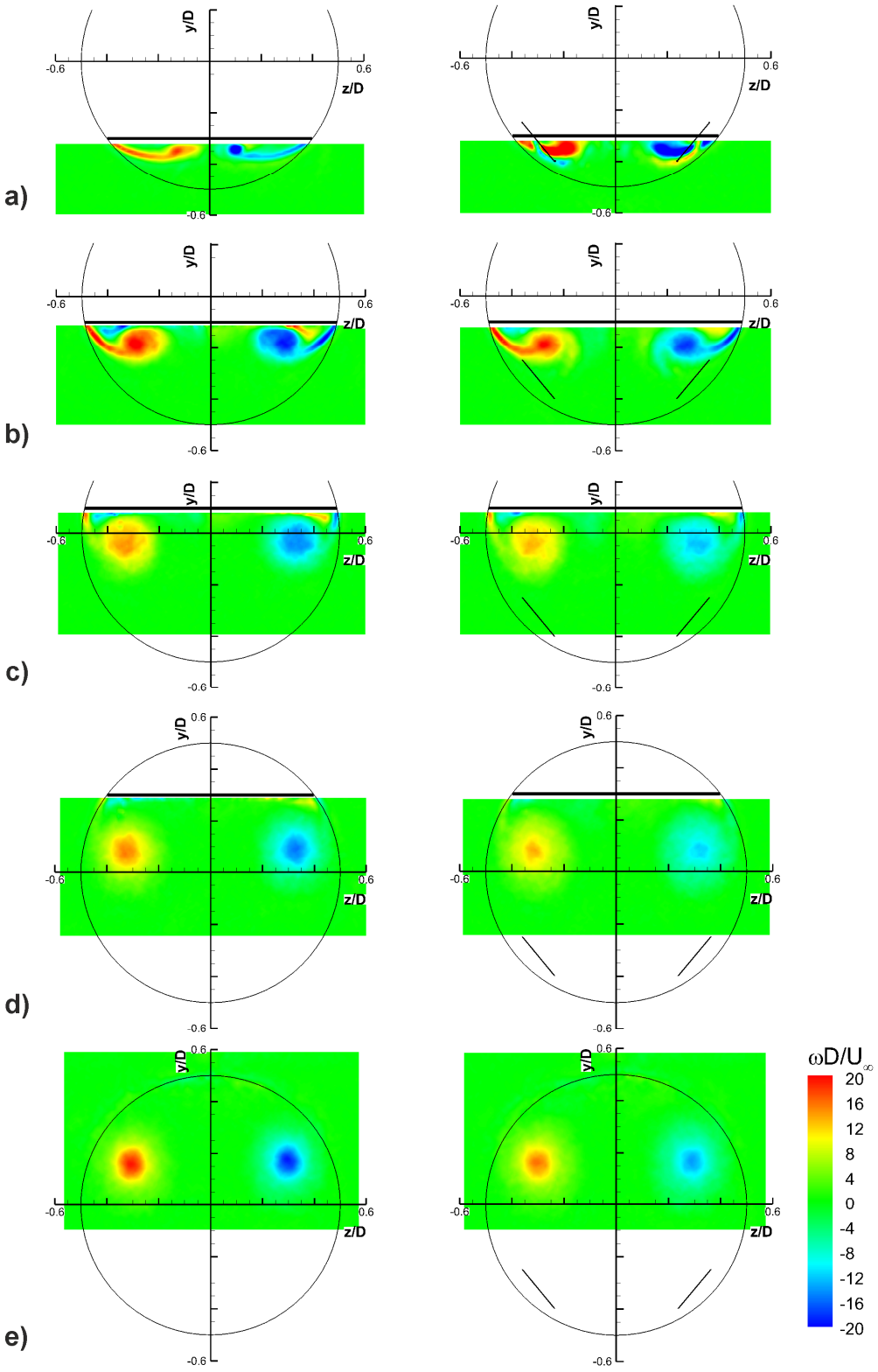

Figure 15. Time-averaged crossflow vorticity of the baseline case, left, and a surface-normal slot jet case, right. Jet slots are indicated by lines on upsweep face. Measurement planes are located at a) x/L = 0.2, b) x/L = 0.4, c) x/L = 0.6, d) x/L = 0.8 and e) x/L = 1.0.

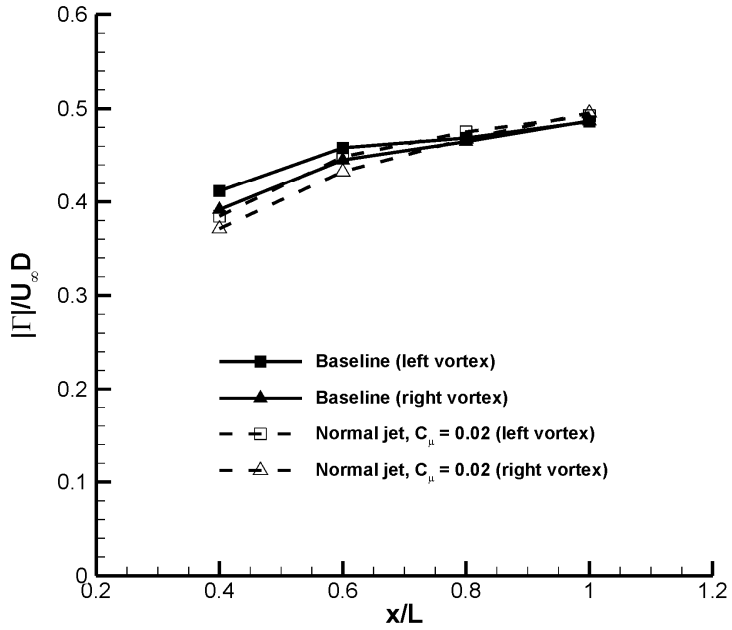

Figure 16. Development of crossflow vortex circulation with streamwise distance for the surface-normal slot jet case.

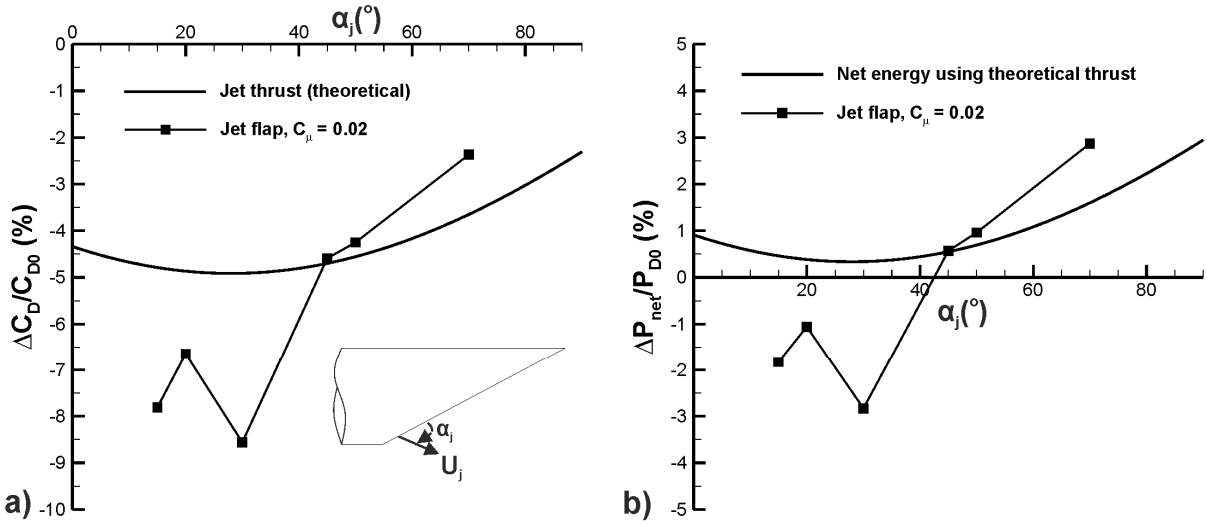

Figure 17. Change in drag coefficient and net energy with α_j for the jet flap case. The theoretical jet thrust is determined by resolving the x-component of C_μ and dividing through by the baseline drag coefficient, C_{D0}.

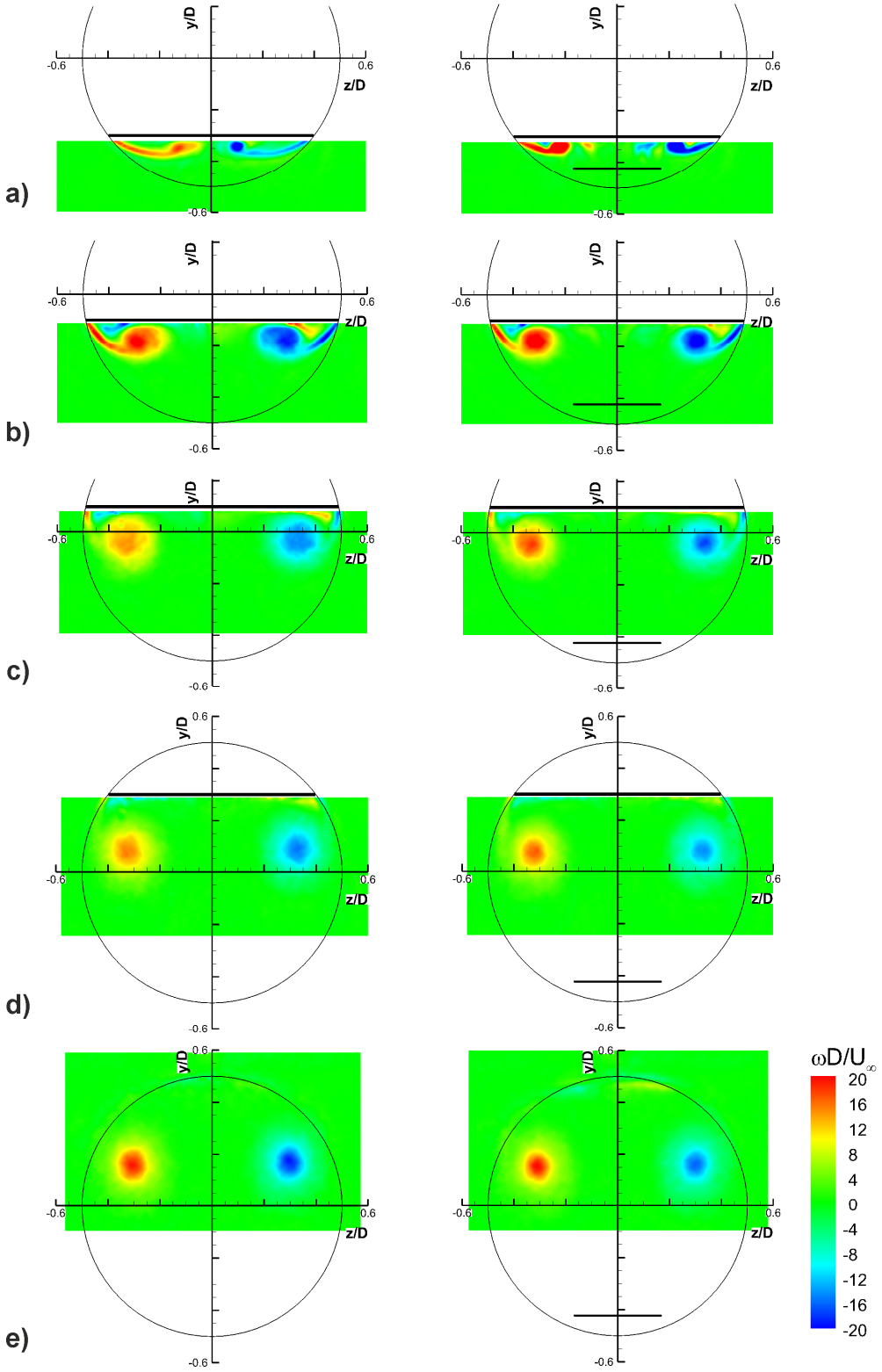

Figure 18. Time-averaged crossflow vorticity of the baseline case, left, and a jet flap case (α_j = 30°), right. Jet flap position is indicated on upswept face. Measurement planes are located at a) x/L = 0.2, b) x/L = 0.4, c) x/L = 0.6, d) x/L = 0.8 and e) x/L = 1.0.

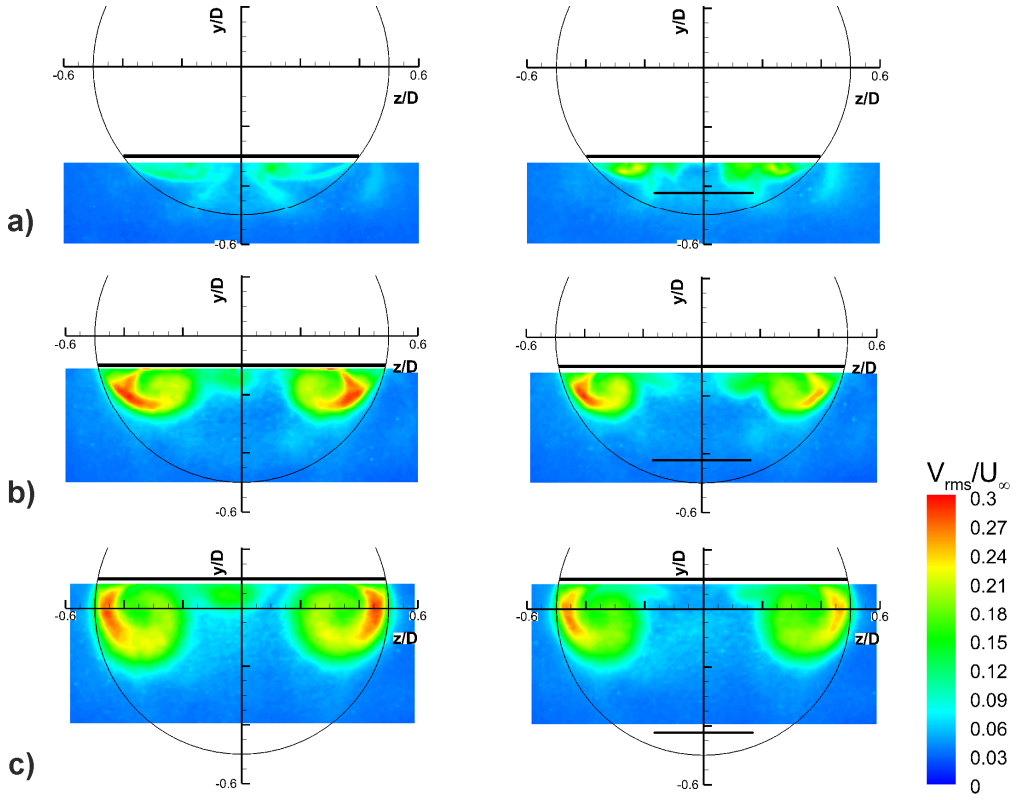

Figure 19. Crossflow turbulence intensity of the baseline case, left, and the jet flap case (α_j = 30°), right. Jet flap position is indicated on upswept face. Measurement planes are located at a) x/L = 0.2, b) x/L = 0.4 and c) x/L = 0.6.

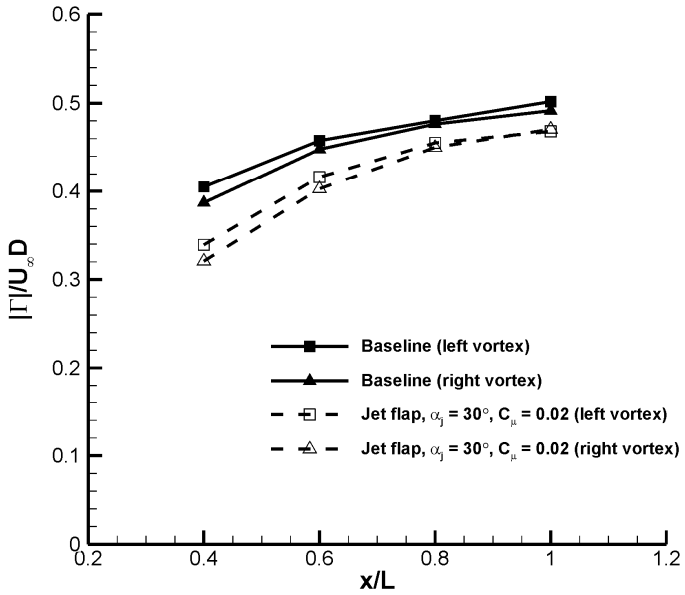

Figure 20. Development of crossflow vortex circulation with streamwise distance for the jet flap case (α_j = 30°).

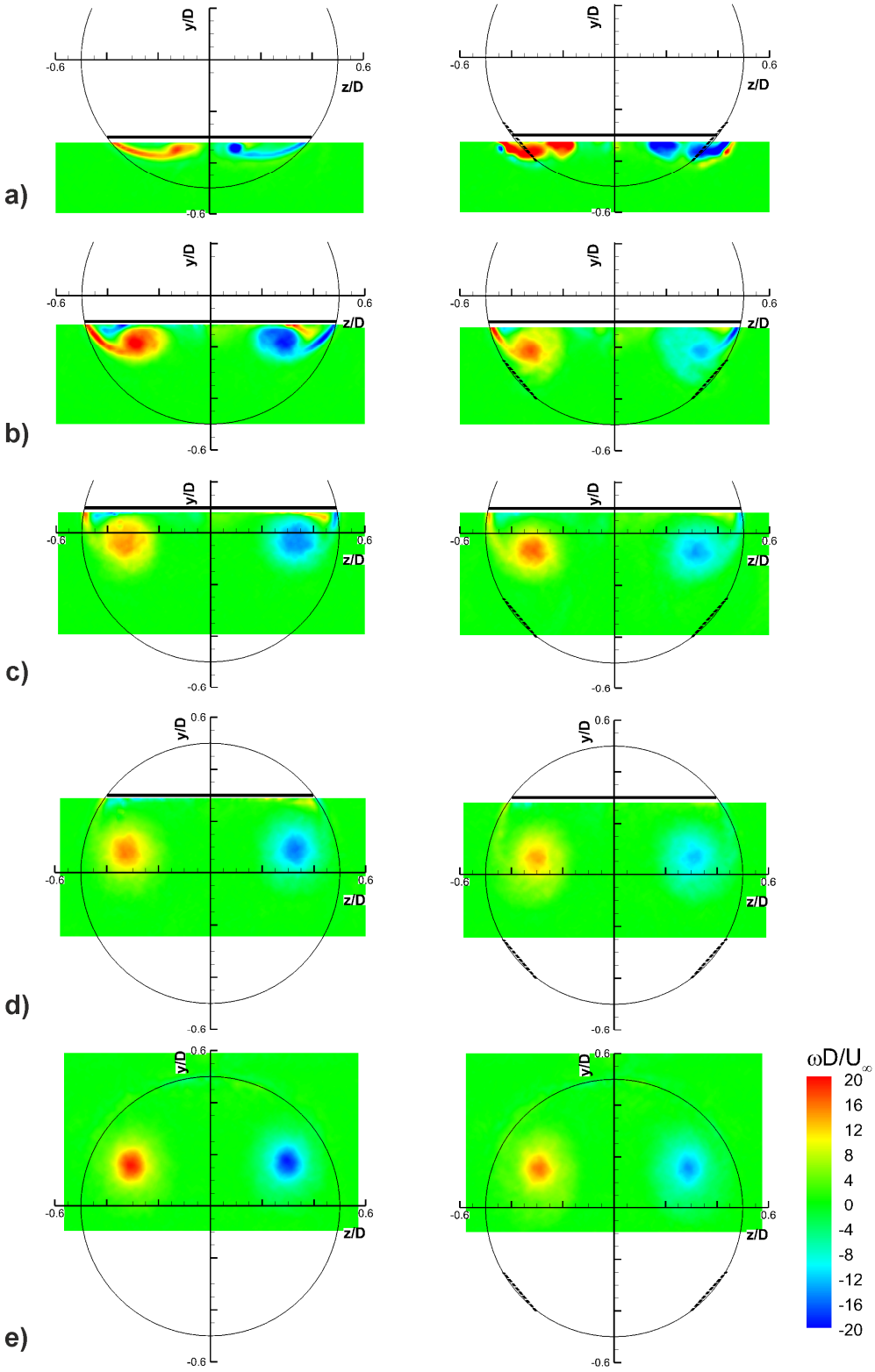

Figure 21. Time-averaged crossflow vorticity of the baseline case, left, and the spanwise slot jet case, right. Jet slots are indicated by dashed lines on upsweep edge. Measurement planes are located at a) x/L = 0.2, b) x/L = 0.4, c) x/L = 0.6, d) x/L = 0.8 and e) x/L = 1.0.

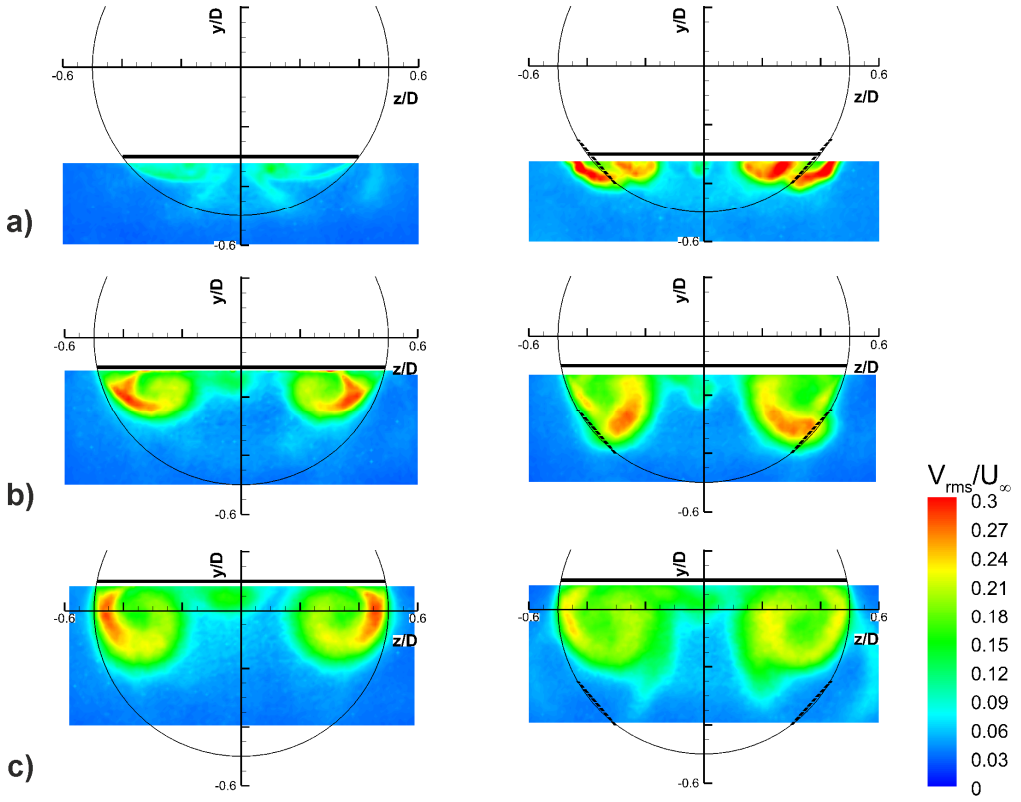

Figure 22. Crossflow turbulence intensity of the baseline case, left, and the spanwise slot jet case, right. Jet slots are indicated by dashed lines on upsweep edge. Measurement planes are located at a) x/L = 0.2, b) x/L = 0.4, and c) x/L = 0.6.

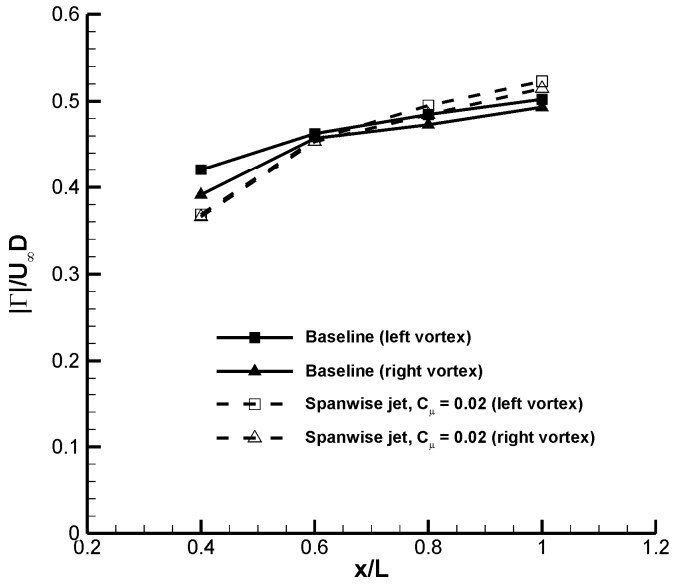

Figure 23. Development of crossflow vortex circulation with streamwise distance for the spanwise slot jet case.